

Polytype switching by super-lubricant van der Waals cavity arrays

<https://doi.org/10.1038/s41586-024-08380-2>

Received: 18 July 2024

Accepted: 8 November 2024

Published online: 5 February 2025

 Check for updates

Youngki Yeo¹, Yoav Sharaby¹, Nirmal Roy¹, Noam Raab¹, Kenji Watanabe², Takashi Taniguchi³ & Moshe Ben Shalom¹✉

Expanding the performance of field-effect devices is a key challenge of the ever-growing chip industry at the core of current technologies¹. Non-volatile multiferroic transistors that control atomic movements rather than purely electronic distribution are highly desired². Recently, a field-effect control over structural transitions was achieved in commensurate stacking configurations of honeycomb van der Waals (vdW) polytypes by sliding boundary strips between oppositely polarized domains^{3–6}. This ferroelectric hysteretic response, however, relied on pre-existing dislocation strips between relatively large micron-scale domains, severely limiting practical implementations^{3,7,8}. Here we report the robust electric switching of single-domain polytypes in nanometre-scale islands embedded in super-lubricant vdW arrays. We etch cavities into a thin layered spacer and then encapsulate it with functional flakes. The flakes above/under the lattice-mismatched spacer sag and touch at each cavity to form islands of commensurate and metastable polytype configurations. By imaging the polarization of the polytypes, we observe nucleation and annihilation of boundary strips and geometry-adaptable ferroelectric hysteresis loops. Using mechanical stress, we further control the position of boundary strips, modify marginal twist angles and nucleate patterns of polar domain. This super-lubricant arrays of polytype (SLAP) concept suggests ‘slidtronics’ device applications such as elastic-coupled neuromorphic memory cells and non-volatile multiferroic tunnelling transistors and programmable response by designing the size, shape and symmetry of the islands and of the arrays⁹.

Unlike electronic transitions, crystalline structural transitions are challenging to control owing to considerable energy barriers associated with breaking solid bonds at ambient conditions, away from the lattice melting temperature. Nevertheless, some materials may exhibit practical transitions between amorphous and crystalline orders in response to external stimuli such as optical or electric pulses¹⁰. Switching the discrete periodic symmetries in these ‘phase-change’ materials directly affects their collective lattice excitations and numerous subsequent properties. Thus, electric control of structural transitions enables, in principle, switching of intrinsic responses such as light emission, conductivity and magnetic order in so-called multiferroic devices¹¹.

Exceptional electric-field switching between vdW polytypes with discrete commensurate stacking configurations that break inversion and mirror symmetry was recently demonstrated^{12–14}. Owing to relatively weak interlayer adhesion and high planar stiffnesses, partial dislocations strips between domains with opposite structural and polar orientations elongate and slide³ to expand better-stable configurations of co-aligned polarization P_z . These stacking-fault dislocation strips in polytypes of honeycomb graphene¹⁵, hexagonal boron nitride¹⁶ (h-BN) or transition metal dichalcogenides¹⁷ (TMDs), are about 30 atoms wide, as determined by the Burgers vector in the partial dislocation (one bond length),

the potential-well energy in the commensurate state (about one meV per atom) and the planar elastic modulus¹⁸ (approximately 1 TPa). The energy cost of these dislocation strips owing to the separation and planar strain of the extra layers is about 1 eV per nm length¹⁶. Thus, electric nucleation of a boundary strip that crosses the system, an essential step for structural transition, is restricted at room temperature (below the turbostratic transition¹⁹), even if cutting the structure into small nanoscale islands and applying the external field locally³. Apparently, the open dangling bonds at the physical edges of the layers tend to zip the layers together and restrict interlayer motions⁷. As a result, previous electric hysteresis measurements have relied on pre-existing dislocations in micrometre-sized structures^{3,7,8,20,21}. Further challenges arising in mechanically assembled interfaces are uncontrollable twists and stiff moiré networks that suppress the sliding motion and restrict local switching. Moreover, after removing the external field, the rigid strip network pulls the moiré pattern back to its initial dimensions and hence eliminates the desired hysteretic memory response^{7,22}.

The SLAP concept reported here overcomes these challenges by embedding tiny commensurate islands in an incommensurate super-lubricant medium. It enables electrical-domain nucleation and subsequent switching of nanoscale single-polytype islands. Given

¹School of Physics and Astronomy, Tel Aviv University, Tel Aviv, Israel. ²Research Center for Electronic and Optical Materials, National Institute for Materials Science, Tsukuba, Japan. ³Research Center for Materials Nanoarchitectonics, National Institute for Materials Science, Tsukuba, Japan. ✉e-mail: moshebs@tauex.tau.ac.il

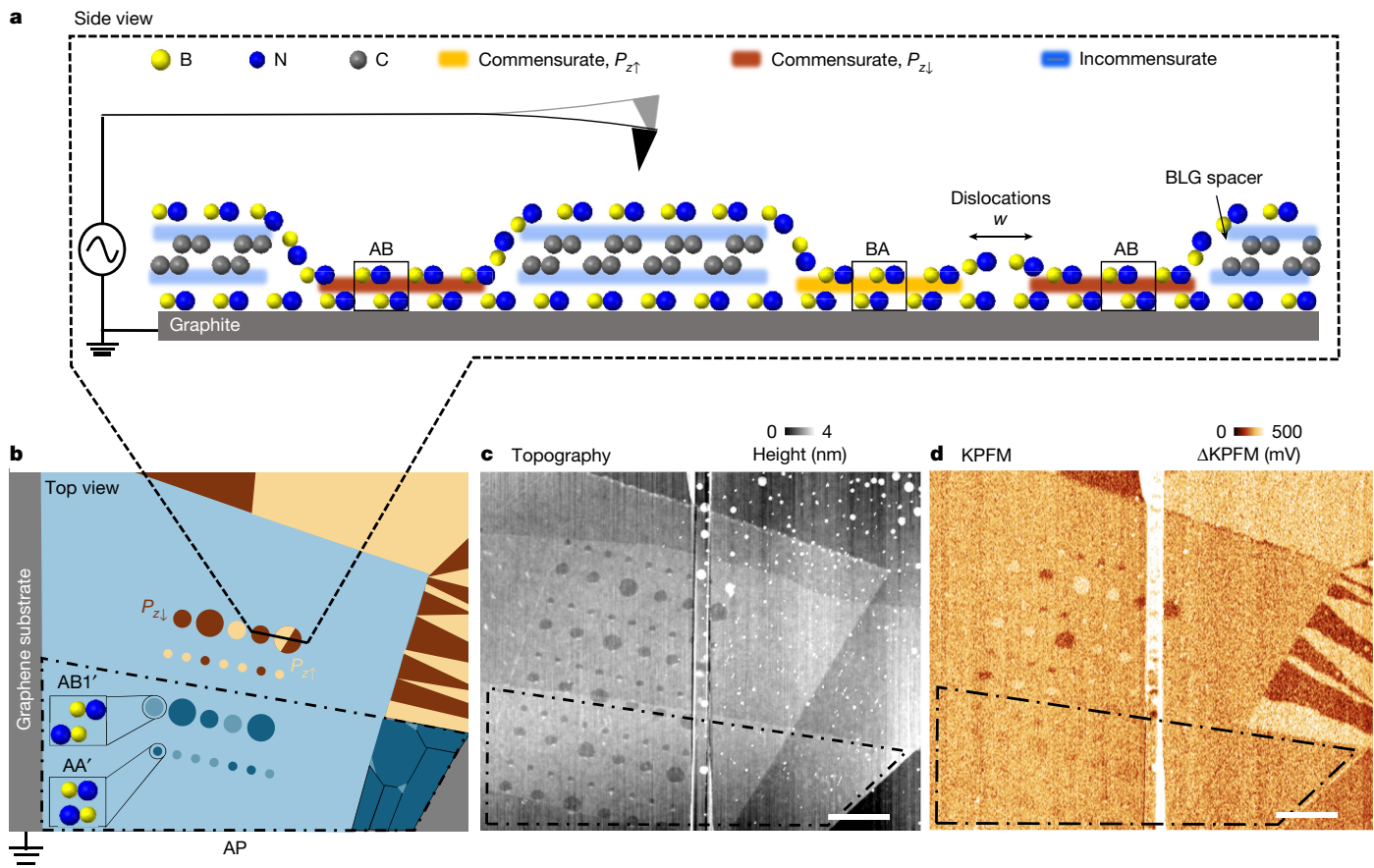


Fig. 1 | Super-lubricant array of vdW polytypes (SLAP). **a,b**, Side view and top view device illustrations. The linecut shows a pair of cavities etched in a bilayer graphene spacer (identical carbon spheres) and encapsulated by two parallel h-BN layers (yellow and blue spheres). Commensurate h-BN interfaces of AB/BA polytype configurations at the cavities are shaded with dark/bright brown colour for down/up internal polarizations. Lubricant incommensurate interfaces with the spacer are shaded in cyan. The right-side cavity island shows mixed BA/AB

domains separated by a w -wide partial dislocation strip. The dashed-dotted line borders a region of antiparallel AA' and AB1' polytypes¹¹ islands marked by dark blue and bright blue colours, respectively. **c**, Topographic image of device 1 with 2-nm-thick parallel h-BN flakes. Note the brighter (one layer thicker) surface below the dashed-dotted line. **d**, Corresponding electric surface potential map by KPFM. Scale bars, 1 μm.

the polytype-dependent electronic phases reported so far, such as cumulative polarizations^{23–25}, superconductivity²⁶, spin²⁷, orbital²⁸ and topological orders²⁹, the structural switching of SLAP islands by electric field offers appealing multiferroic control mechanisms for subsequent electronic responses⁹.

Superlubricity-mediated sliding

The main idea behind our SLAP devices is to: (1) squeeze the active polytype interface into small cavity islands with lower dislocation nucleation energy costs but without physically cutting the functional layers and introducing open edge bonds (see Fig. 1) and (2) use lattice-mismatched or considerably twisted layered spacers to enable superlubricant motion outside the active islands that further support dislocation nucleation. These ‘not-active’ incommensurate regions between the cavities eliminate the stiff topological networks of boundary dislocations between commensurate domains that suppress the sliding and prevent switching^{9,15}. Moreover, these regions facilitate exceptionally high sliding lubricity with record-low approximately 10^{-5} friction coefficients^{30–32} and hence mediate long-range elastic interactions between the cavities, which are typically restricted by any pinning barrier. For example, the commensurate pinning barrier that prevents superlubricity $E_{sp} \approx 1$ meV per atomic area confines the planar strain relaxation range to a few-nanometres-wide boundary strip only. This range (or strip width) $w = \frac{a}{2} \sqrt{\frac{k}{E_{sp}}} \approx 7$ nm (refs. 15,33) is determined by

minimizing the planar elastic energy to about $\frac{1}{4}k\frac{a^2}{w}$ ($k \approx 150$ N m⁻¹ the shear stiffness, $a \approx 0.14$ nm the bond length) and the misalignment energy cost to about wE_{sp} . Therefore, planar stress fields emerging in layers that are part of a super-lubricant interface with residual pinning much below E_{sp} may extend substantially beyond w and elastically couple adjacent islands⁹.

Figure 1 shows cross-sectional and top views of the super-lubricant array concept using a graphene spacer and functional h-BN flakes. We etch circular cavities into a graphene bilayer (BLG; see the identical carbon spheres in Fig. 1a) using the electrode-free local anodic oxidation method³⁴ (see Methods). Then, we encapsulate the BLG with h-BN layers (blue and yellow spheres, respectively) that sag to touch at the cavity position, forming aligned commensurate AB or BA interfaces (dark/bright brown shaded). These stable polytype configurations break inversion and mirror symmetry as shown by the unit cells line-cuts along the armchair direction (see rectangular frames), inducing vertical polarization at this active interface. Outside the cavity, on the other hand, the h-BN/graphene interfaces are incommensurate owing to lattice mismatch and finite twist angle (blue-shaded interfaces). Figure 1b shows a top view of a cavity array design with various cavity diameters and inter-cavity spaces. Outside the blue-shaded spacer (top-right side), triangular domains of AB and BA configuration form, with opposite structural orientations and internal polarizations P_z (noted by bright/dark colours)³. Islands of non-polar AA' and AB1' polytypes that preserve inversion symmetry (also illustrated) appear

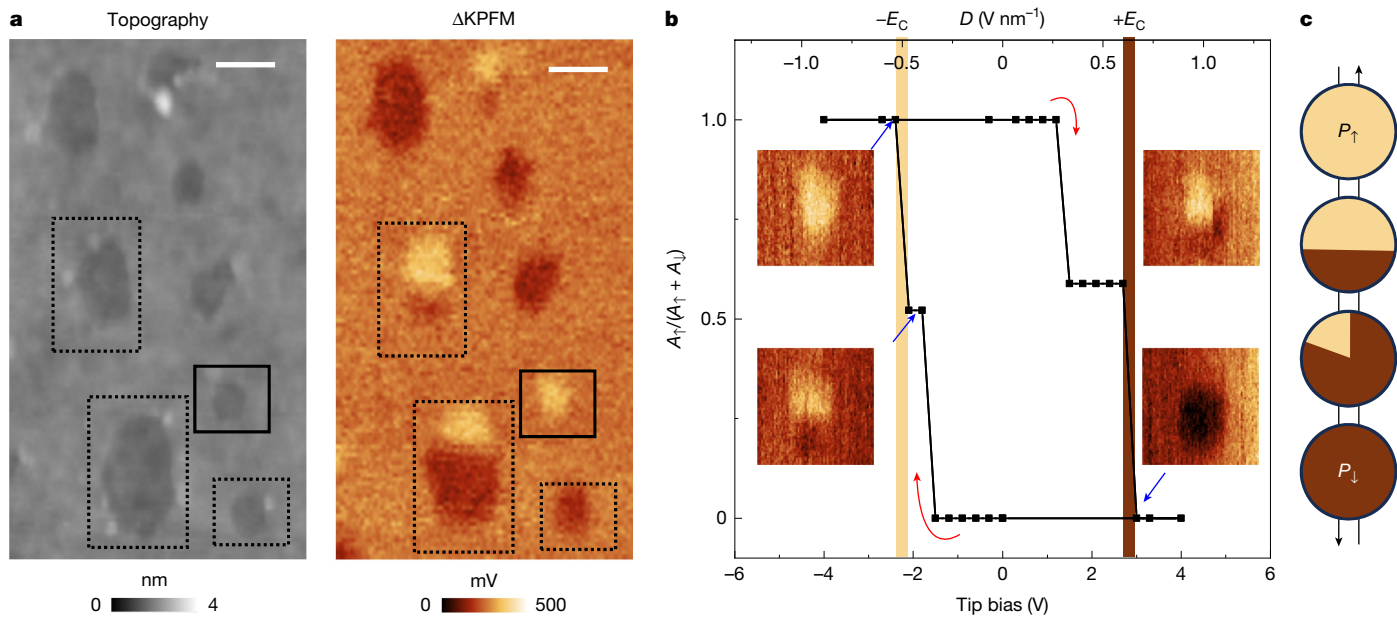


Fig. 2 | Electric-field-induced dislocation nucleation and annihilation. **a**, AFM topography and surface potential maps of device 2, with h-BN functional layers, before electric-field poling. Scale bars, 200 nm. **b**, The relative bright domain area (A_\uparrow) in the 150-nm cavity marked by a solid line frame in **a**, as a function of the tip bias during the electric poling scan before imaging.

The coercive switching fields are indicated by bright/dark bars. Full hysteresis loops of all marked cavities are shown in Extended Data Figs. 3 and 4. **c**, Illustration of intermediate domain structures observed in the experiments (see Extended Data Fig. 5).

in regions of antiparallel functional layers as expected for an extra (rotated) interfacial layer¹⁴ (dashed-dotted line frame, top view).

Imaging switching by surface potential

To monitor the cavity polytypes, as a ferroelectric case study, we use flakes of h-BN or WSe₂ as the functional encapsulating crystals (see devices 1–3 details in Methods, Extended Data Table 1 and Extended Data Fig. 1). A parallel commensurate stacking of these binary compounds spreads the electrons unequally between the top and bottom layers, inducing interfacial-confined polarization P_z . Each interfacial shift by a single inter-atomic distance switches the untwisted AB stacking to BA and vice versa, which is equivalent to switching the interface and P_z upside down¹² (see rectangular frames in Fig. 1a). Hence, monitoring P_z is an exceptional sensor for minute interfacial shear motions, with opposite P_z orientation in adjacent AB/BA modifying the electric surface potential by $\Delta V \approx 240$ and 120 mV for h-BN and WSe₂, respectively^{3,5,14}, allowing us to distinguish each polytype configuration. Figure 1c presents an atomic force microscopy (AFM) topography map of the device structure illustrated in Fig. 1a,b. We cut the graphene spacer with straight borders, punctured 300-nm, 200-nm, 100-nm and 20-nm cavity diameters and used 2-nm-thick flakes of functional h-BN (see darker circles and further details in Methods and Extended Data Fig. 2).

The surface potential map, measured by Kelvin probe force microscopy (KPFM; see Methods) is presented in Fig. 1d. Outside the spacer, at the top and right sides of the map, bright/dark domains differing by 240 mV potential steps confirm the formation of polar AB and BA interfaces. Notably, the same bright/dark circles at the location of the cavity reveal uniform single-domain polytypes embedded in uniform spacer potential. A similar response is observed in device 2 with a monolayer graphene spacer and h-BN functional flakes (Fig. 2 and Extended Data Figs. 1 and 3–7) and device 3 with a trilayer graphene spacer and WSe₂ monolayers as the functional flakes (Fig. 3 and Extended Data Fig. 1). We note that all cavities above the dashed dark line in Fig. 1d appear either bright or dark. Conversely, below this line, the potential at the cavities and outside the spacer is measured to be the average

potential as expected for non-polar antiparallel interfaces. The topography map in this section confirms an extra h-BN layer in the bottom flake (7/6, 7/5 layers in the top/bottom flake below/above the dashed line, respectively) and the formation of mirror-symmetric AA' or AB1' interfaces^{3,14} (as in the naturally grown 2H flakes; see framed illustration in Fig. 1b). Overall, the topography and potential maps confirm commensurate interface formations in pristine cavity arrays spanning many μm^2 regions, released from external contaminations, even at the circular edges of the spacer.

Dislocation nucleation and annihilation

To explore the cavities switching dynamics, we applied external displacement fields between the atomic force microscope tip and a bottom graphite electrode using bias contact scanning mode (see Methods). A set of poling and then imaging maps are taken above representative cavities with different diameters (Fig. 2a). Figure 2b shows surface potential maps of a 150-nm-wide cavity after increasing/decreasing the poling bias by 0.3-V steps, corresponding to electric-displacement-field steps of 0.06 V nm^{-1} . Notably, a new dislocation strip nucleates at approximately $\pm 0.3 \text{ V nm}^{-1}$ and then slides at a coercive field $E_c \approx \pm 0.6 \text{ V nm}^{-1}$ to entirely switch the cavity between uniform single domains of up-polarization and down-polarization. Although previously reporting smaller coercive fields of roughly 0.3 V nm^{-1} , we note that these experiments³ could only slide pre-existing dislocation strips without nucleating new strips up to displacement fields as high as 1.5 V nm^{-1} and dielectric breakdown.

To analyse the hysteresis loop and the intermediate polarization states, we plot the relative coverage of up (bright) domains, $A_\uparrow/(A_\uparrow + A_\downarrow)$. A complete set of maps is shown in Methods and Extended Data Fig. 3 and was repeated over five switching cycles. The hysteresis loops of three more cavities marked by dashed frames in Fig. 2a are presented in Methods and Extended Data Fig. 4. Although the 150-nm and 250-nm cavities show similar hysteresis windows, we could only switch the 350-nm cavity partially under electric displacements as high as 1 V nm^{-1} (before the sample is damaged). In all cavities, the centre

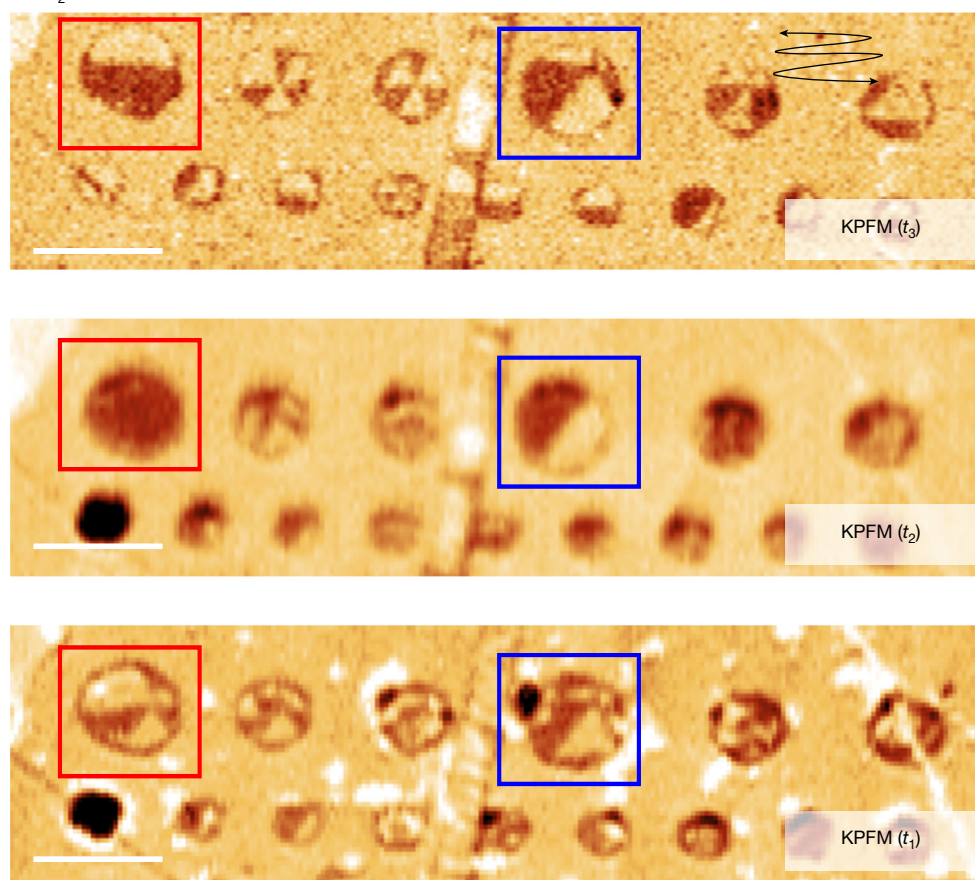
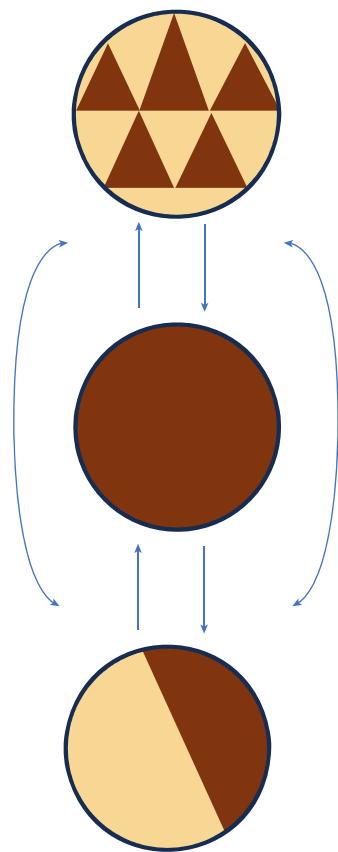
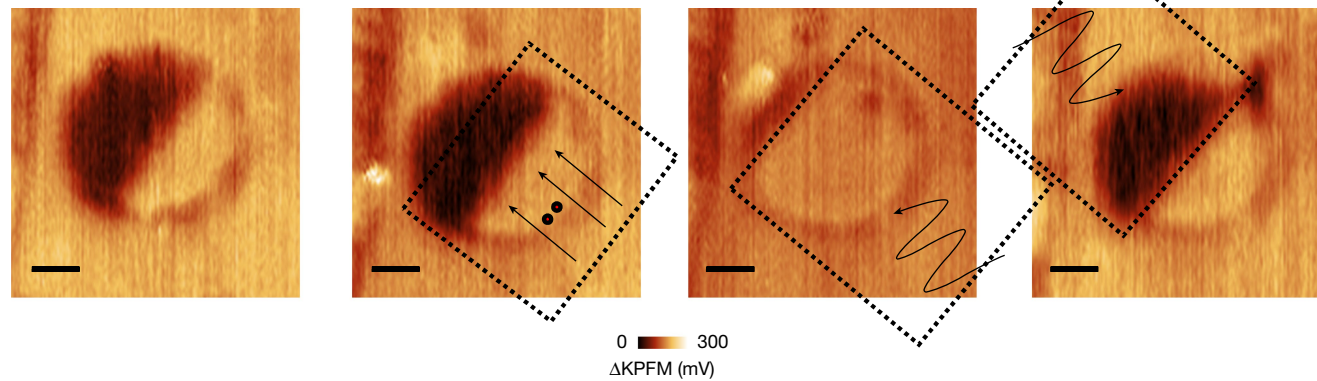
a**b****c** Initial domain

Fig. 3 | Mechanical nucleation and reconfiguration of confined domain patterns. **a**, Surface potential maps of device 3 with functional WSe₂ monolayers before and after contact-mode scans at a tip force of 300 nN. Black arrows show the orientation of the slow and fast contact-scanning axes before the non-contact imaging. Scale bars, 500 nm. **b**, Schematic illustration of the cavity topologies observed, including single, two and multiple domains of

twisted moiré patterns. **c**, Surface potential maps taken after pressure scanning the regions marked by dashed frames. Scanning the fast axes perpendicular to the boundary strip in the forward direction only (straight arrows) does not change the final pattern, whereas back and forward scanning of the fast axes along the strip (armchair) direction (curved arrows) controls the boundary position accurately and reversibly. Scale bars, 100 nm.

of the hysteresis loop shifts to positive or negative potentials with no apparent sign preference. Because vertical electric fields from the asymmetric tip/graphite electrodes or flexoelectric effects should show sign preference³⁵, we attribute the random shifts to elastic coupling with adjacent cavities and remote pinning by nearby contaminants. We also find strip elongations aligning with the smaller width axes of the oval-shaped cavities (see the two bottom-left cavities in Fig. 2a). Such tendency to shrink the strip length and to snap many cavities into single domains (see Fig. 1d) confirms that releasing the strain to the lubricant

interfaces is energetically favourable. Occasionally, we find intermediate triangular domains snapping into 120° or 180° head angles rather than straight boundary strips (see the illustration in Fig. 2c, Methods and Extended Data Fig. 5).

Mechanical switching and twists

Mechanical nucleation and reconfiguration of domain boundaries were previously observed under vertical loads as low as 600 nN in oxide

ferroelectric films³⁶ and 400 nN in the case of pre-existing dislocation strips between non-polar graphitic polytypes³⁷. Dislocation nucleation and domain switching required more intensive mechanical loads exceeding 40 μ N (ref. 38). Even greater nucleation challenges appear in twisted interfaces owing to the rigid moiré network and topologically defined number of alternating domains for a given global twist angle¹⁵. Once the planar relaxation clicks the layers into commensurate domains, the external stress impact becomes irreversible^{39,40}.

To assess the mechanical switching dynamics in SLAP devices, we scanned the arrays in AFM contact mode while applying vertical pressures of 50–300 nN and keeping the slow-axis scan direction parallel to the underlining armchair direction (see Methods). Figure 3a presents three surface potential maps of device 3 (with WSe₂ as active layers) measured before and after applying a vertical pressure of 300 nN at times t_1 , t_2 and t_3 . Notably, the domain patterns modify between the scans in nearly all cavities. The red/blue rectangles mark relatively large cavities in which triangular domains are tuned to a single/double domain pattern and back, respectively, as illustrated in Fig. 3b. We find a threshold load for domain nucleation and motion of around 200 nN (Fig. 3), corresponding to a pressure of about 161 MPa (see Methods and Extended Data Fig. 6) on a roughly 1,000 nm² effective tip diameter and a planar shear force of below 30 nN measured by the horizontal deflections of the tip (as measured by the horizontal deflections of the tip; Extended Data Fig. 8).

We note the 100-nm triangular domains appearing in device 3 owing to a twist angle of about 0.1° between the active layers, whereas devices 1 and 2 show more uniform islands. We attribute the triangular domains in this device (rather than snapping into uniform islands) to a larger residual pinning potential, as well as the twist angle. This domain pattern further depends on the cavity dimensions and the distance to nearby cavities that also pin down the moiré network. In some cases, we could push and pin down the dislocation strip within the cavity by scanning the fast axes along the strip axes. Figure 3c shows such a strip that precisely follows the end position of the scanning pattern.

Conclusions and outlook

Although the reported SLAP devices behave as exceptionally sensitive strain detectors, with any mechanical shift by one atomic spacing changing the cavity colour in the potential map, we find the electric switching of uniform polytypes within each island to be the main observation reported here. The electric nucleation of boundary strips that slide spontaneously to annihilate at the island boundary and switch uniform polype configurations implies efficient device concepts that were practically out of reach so far. Moreover, coercive switching fields that depend on the island dimensions and the long-range elastic coupling to adjacent cavities in the array suggest new tools to design the overall switching dynamics and response. It extends naturally to various vdW polytypes, in which correlated electronic orders such as magnetism couple to the structural phase to provide further multiferroic properties⁹.

Online content

Any methods, additional references, Nature Portfolio reporting summaries, source data, extended data, supplementary information, acknowledgements, peer review information; details of author contributions and competing interests; and statements of data and code availability are available at <https://doi.org/10.1038/s41586-024-08380-2>.

1. International Roadmap for Devices and Systems. *IEEE* <https://doi.org/10.60627/0p45-zj55> (2023).
2. Wuttig, M. & Yamada, N. Phase-change materials for rewriteable data storage. *Nat. Mater.* **6**, 824–832 (2007).
3. Vizner Stern, M. et al. Interfacial ferroelectricity by van der Waals sliding. *Science* **372**, 1462–1466 (2021).

4. Yasuda, K., Wang, X., Watanabe, K., Taniguchi, T. & Jarillo-Herrero, P. Stacking-engineered ferroelectricity in bilayer boron nitride. *Science* **372**, 1458–1462 (2021).
5. Weston, A. et al. Interfacial ferroelectricity in marginally twisted 2D semiconductors. *Nat. Nanotechnol.* **17**, 390–395 (2022).
6. Wang, X. et al. Interfacial ferroelectricity in rhombohedral-stacked bilayer transition metal dichalcogenides. *Nat. Nanotechnol.* **17**, 367–371 (2022).
7. Ko, K. et al. Operando electron microscopy investigation of polar domain dynamics in twisted van der Waals homobilayers. *Nat. Mater.* **22**, 992–998 (2023).
8. Gao, Y. et al. Tunnel junctions based on interfacial two dimensional ferroelectrics. *Nat. Commun.* **15**, 4449 (2024).
9. Vizner Stern, M., Salleh Atri, S. & Ben Shalom, M. Sliding van der Waals polytypes. *Nat. Rev. Phys.* <https://doi.org/10.1038/s42254-024-00781-6> (2024).
10. Yamada, N. et al. High speed overwritable phase change optical disk material. *Jpn. J. Appl. Phys.* **26**, 61–66 (1987).
11. Cheong, S.-W. & Mostovoy, M. Multiferroics: a magnetic twist for ferroelectricity. *Nat. Mater.* **6**, 13–20 (2007).
12. Li, L. & Wu, M. Binary compound bilayer and multilayer with vertical polarizations: two-dimensional ferroelectrics, multiferroics, and nanogenerators. *ACS Nano* **11**, 6382–6388 (2017).
13. Fei, Z. et al. Ferroelectric switching of a two-dimensional metal. *Nature* **560**, 336–339 (2018).
14. Woods, C. R. et al. Charge-polarized interfacial superlattices in marginally twisted hexagonal boron nitride. *Nat. Commun.* **12**, 347 (2021).
15. Alden, J. S. et al. Strain solitons and topological defects in bilayer graphene. *Proc. Natl. Acad. Sci. USA* **110**, 11256–11260 (2013).
16. Lebedeva, I. V., Lebedev, A. V., Popov, A. M. & Knizhnik, A. A. Dislocations in stacking and commensurate-incommensurate phase transition in bilayer graphene and hexagonal boron nitride. *Phys. Rev. B* **93**, 235414 (2016).
17. Kushima, A., Qian, X., Zhao, P., Zhang, S. & Li, J. Ripples in van der Waals layers. *Nano Lett.* **15**, 1302–1308 (2015).
18. Popov, A. M., Lebedeva, I. V., Knizhnik, A. A., Lozovik, Y. E. & Potapkin, B. V. Commensurate-incommensurate phase transition in bilayer graphene. *Phys. Rev. B* **84**, 045404 (2011).
19. Tang, P. & Bauer, G. E. W. Sliding phase transition in ferroelectric van der Waals bilayers. *Phys. Rev. Lett.* **130**, 176801 (2023).
20. Yasuda, K. et al. Ultrafast high-endurance memory based on sliding ferroelectrics. *Science* **385**, 53–56 (2024).
21. Bian, R. et al. Developing fatigue-resistant ferroelectrics using interlayer sliding switching. *Science* **385**, 57–62 (2024).
22. Li, H. et al. Global control of stacking-order phase transition by doping and electric field in few-layer graphene. *Nano Lett.* **20**, 3106–3112 (2020).
23. Deb, S. et al. Cumulative polarization in conductive interfacial ferroelectrics. *Nature* **612**, 465–469 (2022).
24. Atri, S. S. et al. Spontaneous electric polarization in graphene polytypes. *Adv. Phys. Res.* **3**, 2300095 (2024).
25. Cao, W. et al. Polarization saturation in multilayered interfacial ferroelectrics. *Adv. Mater.* **36**, 2400750 (2024).
26. Zhou, H., Xie, T., Taniguchi, T., Watanabe, K. & Young, A. F. Superconductivity in rhombohedral trilayer graphene. *Nature* **598**, 434–438 (2021).
27. Huang, B. et al. Electrical control of 2D magnetism in bilayer CrI₃. *Nat. Nanotechnol.* **13**, 544–548 (2018).
28. Shi, Y. et al. Electronic phase separation in multilayer rhombohedral graphite. *Nature* **584**, 210–214 (2020).
29. Lu, Z. et al. Fractional quantum anomalous Hall effect in multilayer graphene. *Nature* **626**, 759–764 (2024).
30. Hirano, M. & Shinjo, K. Atomistic locking and friction. *Phys. Rev. B* **41**, 11837–11851 (1990).
31. Dienwiebel, M. et al. Superlubricity of graphite. *Phys. Rev. Lett.* **92**, 126101 (2004).
32. Leven, I., Krepel, D., Shemesh, O. & Hod, O. Robust superlubricity in graphene/h-BN heterojunctions. *J. Phys. Chem. Lett.* **4**, 115–120 (2013).
33. Constantinescu, G., Kuc, A. & Heine, T. Stacking in bulk and bilayer hexagonal boron nitride. *Phys. Rev. Lett.* **111**, 036104 (2013).
34. Li, H. et al. Electrode-free anodic oxidation nanolithography of low-dimensional materials. *Nano Lett.* **18**, 8011–8015 (2018).
35. Gruber, A. et al. Mechanical stress effect on imprint behavior of integrated ferroelectric capacitors. *Appl. Phys. Lett.* **83**, 728–730 (2003).
36. Lu, H. et al. Mechanical writing of ferroelectric polarization. *Science* **335**, 59–61 (2012).
37. Tsuji, T., Irihama, H. & Yamanaka, K. Observation of anomalous dislocation behavior in graphite using ultrasonic atomic force microscopy. *Jpn. J. Appl. Phys.* **41**, 832–835 (2002).
38. Jiang, L. et al. Manipulation of domain-wall solitons in bi- and trilayer graphene. *Nat. Nanotechnol.* **13**, 204–208 (2018).
39. Ribeiro-Palau, R. et al. Twistable electronics with dynamically rotatable heterostructures. *Science* **361**, 690–693 (2018).
40. Yang, Y. et al. In situ manipulation of van der Waals heterostructures for twistronics. *Sci. Adv.* **6**, eabd3655 (2020).
41. Gilbert, S. M. et al. Alternative stacking sequences in hexagonal boron nitride. *2D Mater.* **6**, 021006 (2019).

Publisher's note Springer Nature remains neutral with regard to jurisdictional claims in published maps and institutional affiliations.

Springer Nature or its licensor (e.g. a society or other partner) holds exclusive rights to this article under a publishing agreement with the author(s) or other rightsholder(s); author self-archiving of the accepted manuscript version of this article is solely governed by the terms of such publishing agreement and applicable law.

© The Author(s), under exclusive licence to Springer Nature Limited 2025

Article

Methods

Sample preparation

Our vdW cavity arrays include (top to bottom): h-BN/top functional layer/graphene spacer/bottom functional layer/graphite gate electrode/SiO₂ substrate, assembled using the dry polymer stamping method with either monolayers WSe₂ or few layers h-BN as the functional layers.

Device characterization. In the main text, we present data from three selected devices. Device 1 (Fig. 1), with a 4.3-nm-thick h-BN flake used to pick up active 2.3-nm and 2.0-nm active h-BN flakes and a bilayer graphene spacer. In device 2 (Fig. 2), we used 2.5-nm-thick h-BN to pick up trilayer h-BN (1 nm), monolayer graphene spacer and trilayer h-BN. In device 3 (Fig. 3), we used 4.5-nm-thick h-BN to pick up monolayer WSe₂, graphene spacer and monolayer WSe₂. Thicknesses of the flakes are summarized in Extended Data Table 1 and an optical microscope image of each device is shown in Extended Data Fig. 1. Pick-up h-BN, top layer, graphene spacer and bottom layer are outlined with red, green, blue and orange lines, respectively.

Graphene spacer lithography. The quality of the cavity edges is crucial to minimizing the pinning of dislocation boundary strips. Our best results were obtained using the electrode-free local anodic oxidation lithography method³⁴. Step-by-step procedures are summarized as follows:

1. Choose the wrinkle-free and tape-residue-free graphene monolayer with an optical microscope.
2. A Pt-coated atomic force microscope tip (MikroMasch HQ: NSC35/Pt tip C) was used to clean a $10 \times 10 \mu\text{m}^2$ lithographic area in advance for removing dirt, which is not captured by optical microscopy. Relative humidity was maintained at 60–80% to boost the chemical reaction between the tip and graphene with commercial humidifier.
3. The tip was retracted from the graphene surface to form water bubbles on the tip edge. 10 VAC, 40 kHz were applied in PFM mode (NX10, Park Systems).
4. Using the lithographic option in NX10, a predesigned bitmap image was used to make various shapes. A 100-nN set point was used for each pixel approach. We avoid higher set points, which result in breaking and flipping the graphene edge.
5. After lithography, any remaining oxidized residue and dirt was removed by cleaning the surface using HQ:CSC38/Al BS tip B from MikroMasch. The outer spacer dimensions were cut to about $10 \times 10 \mu\text{m}^2$ using high-intensity pulsed laser light (1,064 nm, in a WITec alpha300 apyron confocal microscope set-up).

A typical AFM topography map and an optical microscopy image of a trilayer graphene spacer are shown in Extended Data Fig. 2a,b. The cavity diameter is reduced to roughly 20 nm, which is related to the tip apex dimensions (see AFM map) and remains free of oxidation residues. By contrast, cutting the spacer with high-intensity pulsed laser light resulted in substantial oxidation rings (see bright rings in Extended Data Fig. 2c) that damaged the device performance. We note that various laser exposure times and beam intensities always resulted in oxidized layers and topographic eruptions at the edges, extending by approximately 1 μm from the centre of the heated area. These oxide layers are not visible in optical microscopy (Extended Data Fig. 2d).

KPFM

KPFM images were acquired under an inert nitrogen environment using a Park NX-Hivac system in sideband mode³. HQ: NSC35/Pt tip C with approximately 150 kHz resonant frequency, 5.4 N m⁻¹ spring constant or B-doped diamond tip HQ:DMD-XSC11 tip B with approximately 110 kHz resonant frequency, 6.5 N m⁻¹ spring constant were used for KPFM measurements. For sideband measurements, the resonant frequency

of the tip was calibrated and then set 2.5 kHz away. The tip was excited by 2 VAC with 9–15-nm set points for all measurements.

Dislocation control by electric fields

To maintain a large contact area between the tip and the surface, we used contact scanning with 161 nN on HQ: NSC35/Pt tip C (apex radius less than 30 nm), 1 Hz scan speed and pixel sizes less than 5 nm at all specified DC voltages. Alternatively, for HQ:DMD-XSC11 tip B (apex radius 100–250 nm), we used 90 nN. The same scan direction was used in all scans.

Size dependence of coercive switching fields. Switching a uniform single-domain cavity into a full oppositely polarized state involves intermediate domain patterns that govern the system response. To reveal the intermediate state pattern, we imaged the surface potential evolution of the cavity after each increment of the external electric field. Extended Data Fig. 3 shows a selected set of images for a 150-nm cavity (see the hysteresis loop of this cavity in Fig. 2). In this case, we used bias increments of about 0.3 V, corresponding to displacement field steps of 0.06 V nm⁻¹, and measured repeatable hysteresis loops five times. The first two maps show a fully polarized cavity after polling beyond the positive/negative coercive fields (as indicated). Starting with a uniform up (bright) polarization in Fig. 2b, the following image (1 V, at time t_3) shows the first bias in which a boundary wall nucleates and a dark domain covering approximately half of the cavity area appears. This domain pattern remains the same up to a 3-V bias, at which the cavity switches to a fully down-polarized state. The following maps show reversible switching along hysteresis loops with a coercive field between $-2.1 \text{ V}_{\text{tip}}$ and $-2.4 \text{ V}_{\text{tip}}$ for up-polarization and a coercive field between $2.7 \text{ V}_{\text{tip}}$ and $3.0 \text{ V}_{\text{tip}}$ for down-polarization.

Extended Data Fig. 4 presents hysteresis loop measurements of the three extra cavities marked by the dashed frames in Fig. 2a. To minimize the pressure effect, we used a large apex radius diamond tip (HQ:DMD-XSC11 tip B) for three additional cavities. The extra 150-nm-sized cavity and the 250-nm-sized cavities exhibit a switching bias window of 5 V, whereas the 350-nm-sized cavity does not switch completely in a window of 8 V. We could switch up-polarization at -4 V but could not achieve complete down-polarization even at 4.5 V . We note that higher field values were avoided because of finite damage observed (in other cavities). We also note an asymmetry in positive and negative coercive fields in different cavities, whereas the overall window remains the same. Because the centre of the switching window shifts from positive to negative potential in different cavities and seems to be smaller for cavities that are further separated from neighbours and pinning contaminants, we attribute this anisotropy to elastic coupling of the cavity to its environment, rather than vertical electric fields arising by flexoelectric response³⁵.

Intermediate switching states. Here a cavity of 250 nm diameter is scanned with a sharp tip ($<30 \text{ nm}$ apex diameter) in Extended Data Fig. 5, allowing better spatial resolution and a more local polling electric field. A biased scan of the single domain map (dark uniform potential, panel b) first opens a 120° triangle domain (bright, panel c), which then extends by 60° to a straight dislocation strip (boundary of dark/bright, panel d). We note that the tip force and bias affect the stability of the intermediate state and that, so far, we were not able to robustly control the triangular intermediate states. We call for further experiments to establish the intermediate domain pattern as a function of the cavity dimensions, shape and elastics coupling to adjacent cavities.

Dislocation control by tip pressing

Twisted angle control can be performed by various methods. For example, nanometre-to-micrometre-sized cantilevers were used to apply external stress to control the twisted layer in other works^{40,42–44}. In this paper, we used commercial HQ: NSC35/Pt tip C (MikroMasch)

with 50–600 nN forces, 1 Hz scan speed and pixel size less than 20 nm. The spring constant was calibrated using the Sader method, which is recommended above 100 kHz resonant frequency, and optical lever sensitivity was calibrated using a single-layer graphene on SiO₂.

Threshold force for boundary strip sliding. To test the threshold pressure for dislocation nucleation and movement, we conducted dragging experiments with an unbiased tip. Extended Data Fig. 6 shows the potential maps of cavity arrays after applying increasingly growing forces to a narrow tip of less than 30 nm apex radius. The first map showing any domain wall motion appears after applying a 200-nN force (marked by blue rectangular frames). Note that variations in the cavity matrix potential are extremely sensitive to any deformation in the array. Contact scanning with 200 nN in the opposite direction reverts the domain pattern in a reversible manner, whereas higher force levels moved the strips into further cavities and to a larger extent (see 250-nN maps). The latter indicates different threshold values in different cavities as naturally expected. Applying forces below the 200 nN threshold value and after performing dragging experiments did not change the potential pattern as expected (see bottom two maps).

Sagging of active layers in pristine cavities. Occasionally, the stamping process resulted in commensurate layers sagging and the appearance of clear polar polytypes only in part of the array. In Extended Data Fig. 7, for example, the topography and surface potential maps show that cavities from the top part of the array are commensurate and polar (see darker cavity colour in topography and bright/dark potential domains). Conversely, the bottom part of the array remains non-polar and exhibits flat topography of suspended cavity membranes or pockets of aggregated contaminations (bright topography regions). In this case, we scanned the array in contact mode with a finite pressure of 300 nN, pushing the active layers to dwell into the vdW adhesion and to push away the self-cleaning contamination pockets. Imaging the array after the several pressured scans confirms clean and commensurate cavities everywhere (see Extended Data Fig. 7c,d). Hence, we note that the surface potential signal is sensitive to the vertical adhesion and the planar interlayer motion.

Effect of shear/friction force around the cavity. Several hundred MPa of shear force is known to switch graphene polytypes⁴⁵. To understand the detailed impact of mechanical switching of dislocations inside the cavities, it is essential to compare the shear forces applied at the edges and within the cavity. The friction force induces torsional movement of the tip, which is reflected in the difference between forward and backward lateral photodiode signals (V). We calibrated the conversion factor ($n\text{N V}^{-1}$) of lateral force by SiO₂ substrate, for which the friction coefficient is known to be 0.08 (ref. 46). Our estimated h-BN friction

coefficient is 0.055 derived from the conversion factor, which is also reported in the AFM friction experiment on h-BN⁴⁷.

The friction to normal load conversion curve measured on atomically flat h-BN flakes is presented in Extended Data Fig. 8a. Topographic and friction force maps are shown in panels b and c, respectively, taken around a cavity at a 300-nN loading force. The brighter signal in panel c indicates that the lateral friction forces are higher at the edge of cavity, reaching about 30 nN compared with about 15 nN in the flat regions. Both values are far below the values reported in previous experiments of mechanical domain nucleation in uniform crystalline flakes (with loading forces exceeding μN (ref. 38)).

Data availability

All of the data in the experiments and analysis that support the findings of this study are included in the main paper and Methods. Any other relevant data are available at <https://doi.org/10.5281/zenodo.14082606> (ref. 48).

42. Wu, H. et al. Direct visualization and manipulation of stacking orders in few-layer graphene by dynamic atomic force microscopy. *J. Phys. Chem. Lett.* **12**, 7328–7334 (2021).
43. Inbar, A. et al. The quantum twisting microscope. *Nature* **614**, 682–687 (2023).
44. Tang, H. et al. On-chip multi-degree-of-freedom control of two-dimensional materials. *Nature* **632**, 1038–1044 (2024).
45. Nery, J. P., Calandra, M. & Mauri, F. Long-range rhombohedral-stacked graphene through shear. *Nano Lett.* **20**, 5017–5023 (2020).
46. Bosse, J. L., Lee, S., Andersen, A. S., Sutherland, D. S. & Huey, B. D. High speed friction microscopy and nanoscale friction coefficient mapping. *Meas. Sci. Technol.* **25**, 115401 (2014).
47. Zhang, X., Yu, K., Lang, H., Huang, Y. & Peng, Y. Friction reduction of suspended multilayer h-BN based on electrostrain. *Appl. Surf. Sci.* **611**, 155312 (2023).
48. Yeo, Y. Polytype switching by super lubricant van der Waals cavity arrays. Zenodo <https://doi.org/10.5281/zenodo.14082606> (2024).

Acknowledgements We thank N. Ravid and I. Malker for laboratory support. K.W. and T.T. acknowledge support from the JSPS KAKENHI (grant numbers 21H05233 and 23H02052) and World Premier International Research Center Initiative (WPI), MEXT, Japan. M.B.S. acknowledges support from the European Research Council under the European Union's Horizon 2024 research and innovation programme ('SlideTronics', consolidator grant agreement no. 101126257) and the Israel Science Foundation under grant nos 319/22 and 3623/21. We further acknowledge the Center for Nanoscience and Nanotechnology of Tel Aviv University.

Author contributions Y.Y. performed the experiments, supported by Y.S., N.Ro. and N.Ra. and supervised by M.B.S. K.W. and T.T. provided the h-BN crystals. All authors contributed to the writing of the manuscript.

Competing interests Ramot at Tel Aviv University Ltd has applied for a patent (US application no. 63/676,819) on some of the technology and materials discussed here, for which Y.Y., Y.S., N.Ra. and M.B.S. are listed as co-inventors.

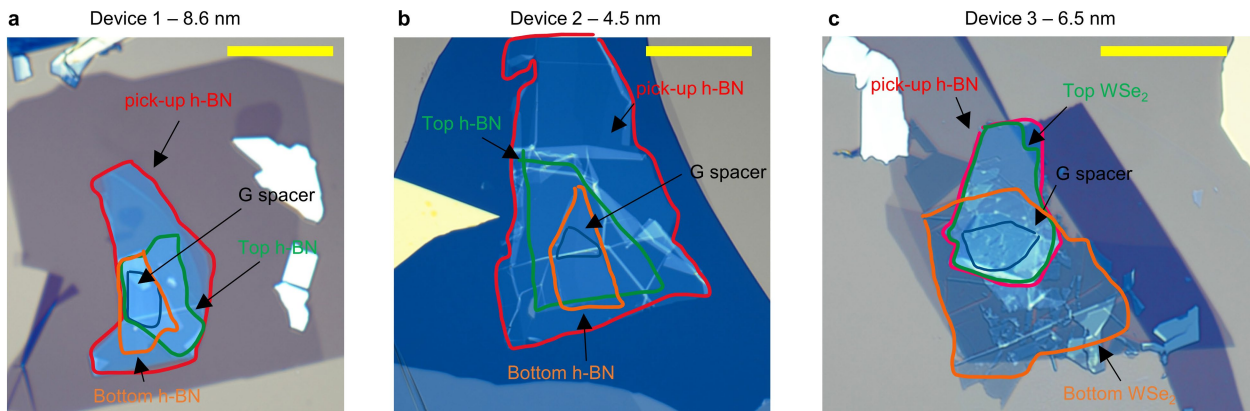
Additional information

Correspondence and requests for materials should be addressed to Moshe Ben Shalom.

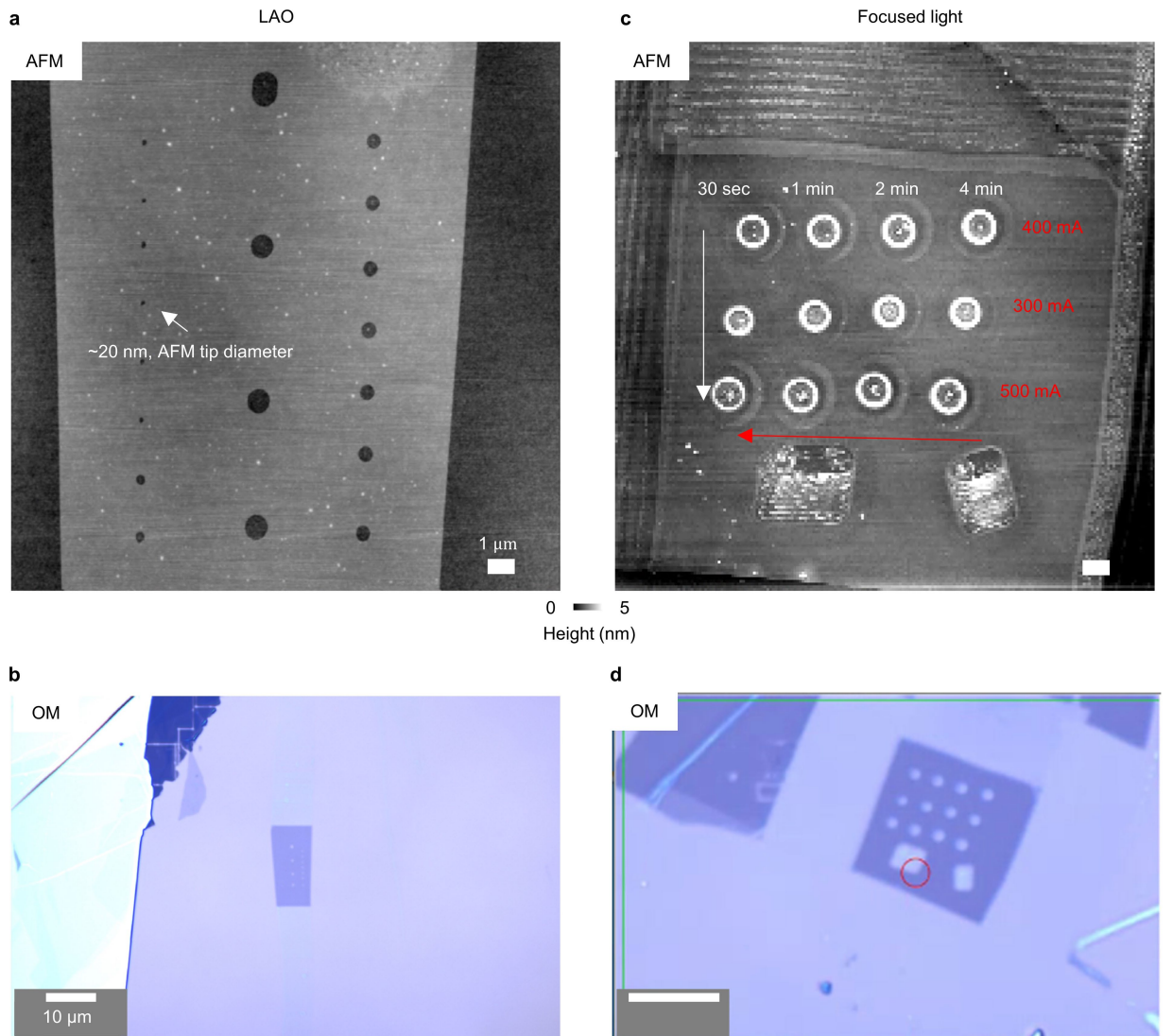
Peer review information *Nature* thanks the anonymous reviewers for their contribution to the peer review of this work.

Reprints and permissions information is available at <http://www.nature.com/reprints>.

Article

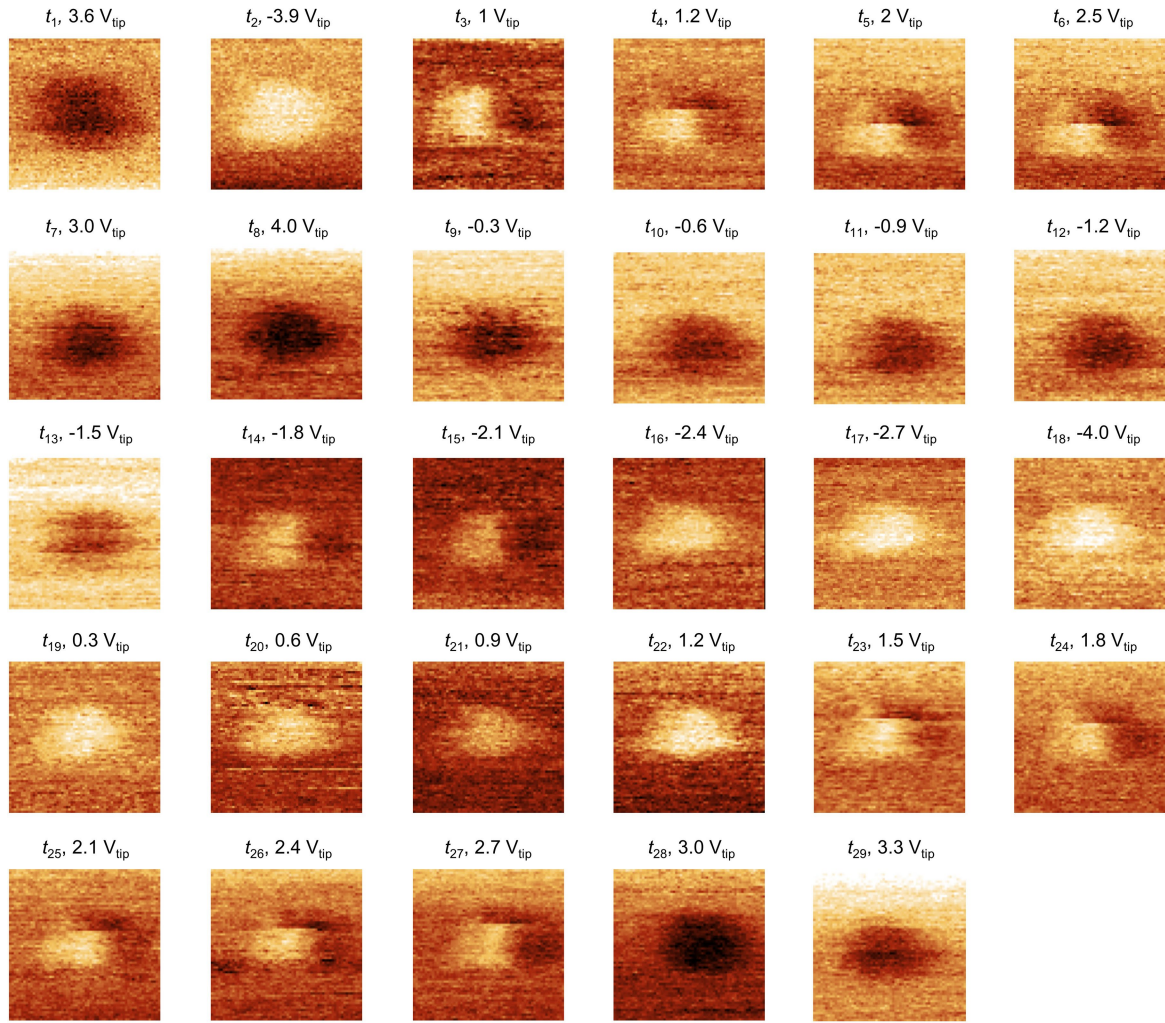


Extended Data Fig. 1 | Optical device images. a–c, Optical microscope image of devices 1–3 presented in Figs. 1–3, respectively. Scale bars, 25 μm .

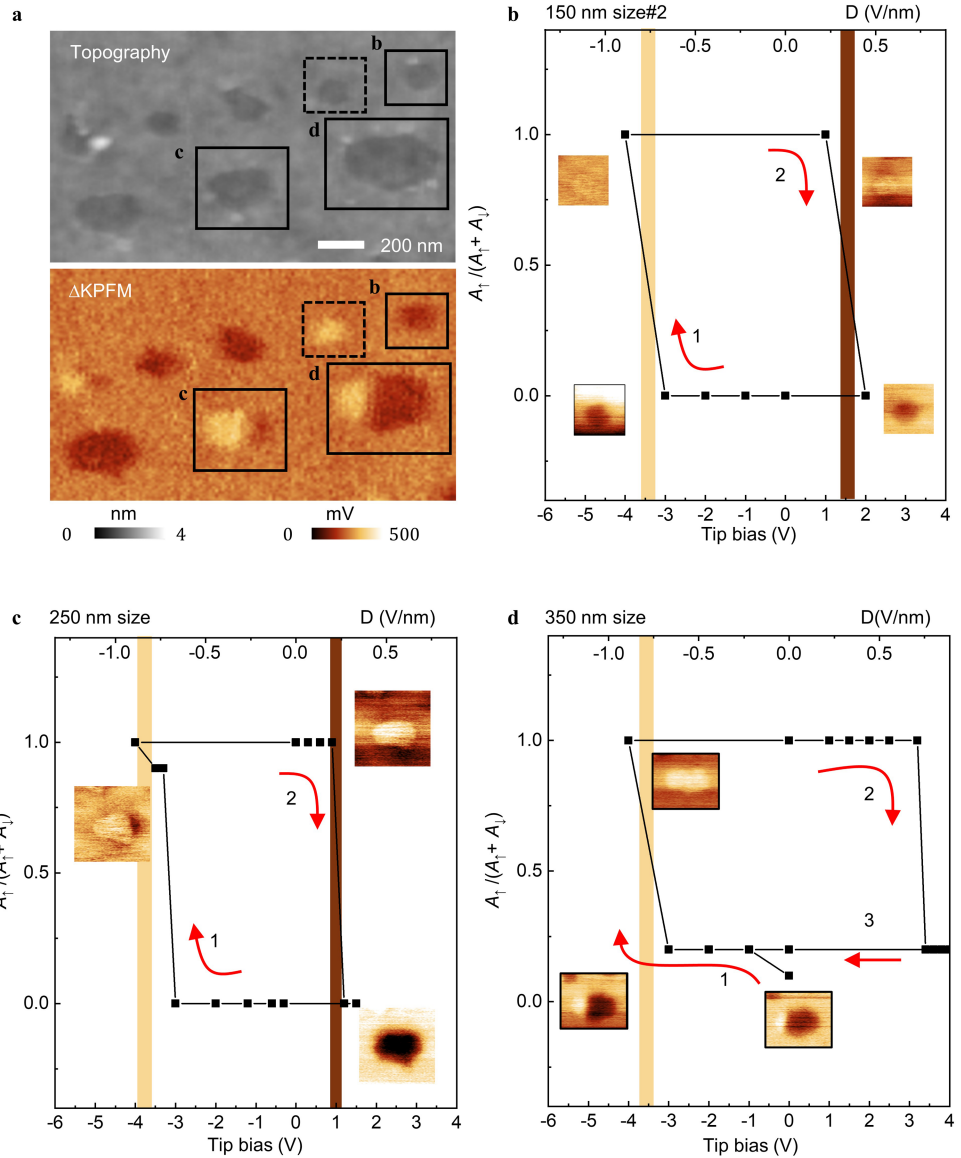


Extended Data Fig. 2 | Comparison of spacer lithography methods. **a,b**, AFM and optical microscope image of local anodic oxidation lithography with cavity diameter down to about 20 nm. **c,d**, AFM and optical image of laser pulse lithography.

Article



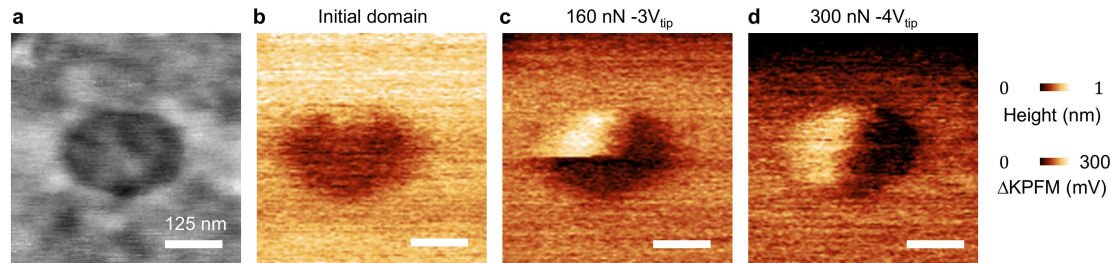
Extended Data Fig. 3 | Imaging ferroelectric hysteresis loop for a 150-nm cavity. Device 2; see Fig. 2. Domain pattern imaged by KPFM after bias scans at the voltage and time indicated on each map.



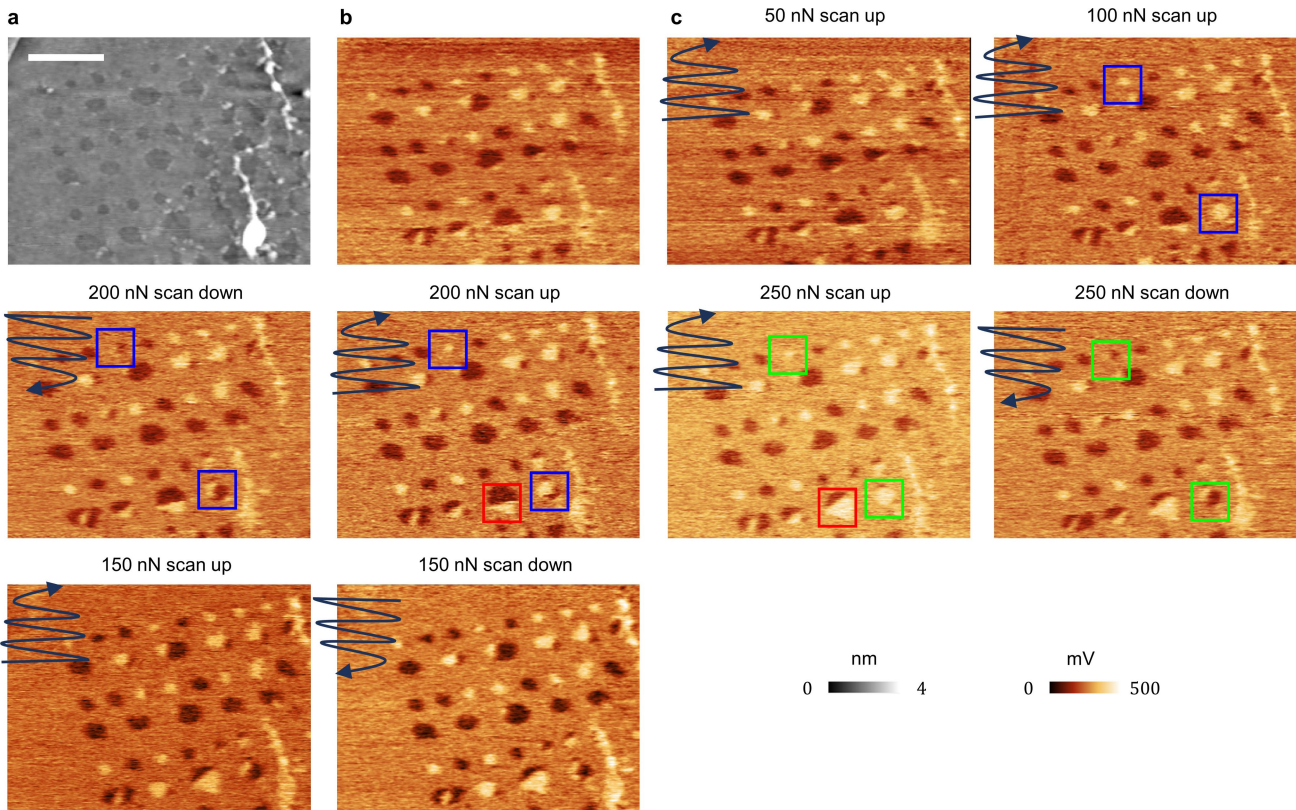
Extended Data Fig. 4 | Further ferroelectric hysteresis measurements (device 2). **a**, Topographic and KPFM maps of the cavity array. **b–d**, Hysteresis loops of the cavities marked in **a**, with diameters of 150, 250 and 350 nm,

respectively. Bright and dark column stands for the switching to complete up-polarization and down-polarization.

Article

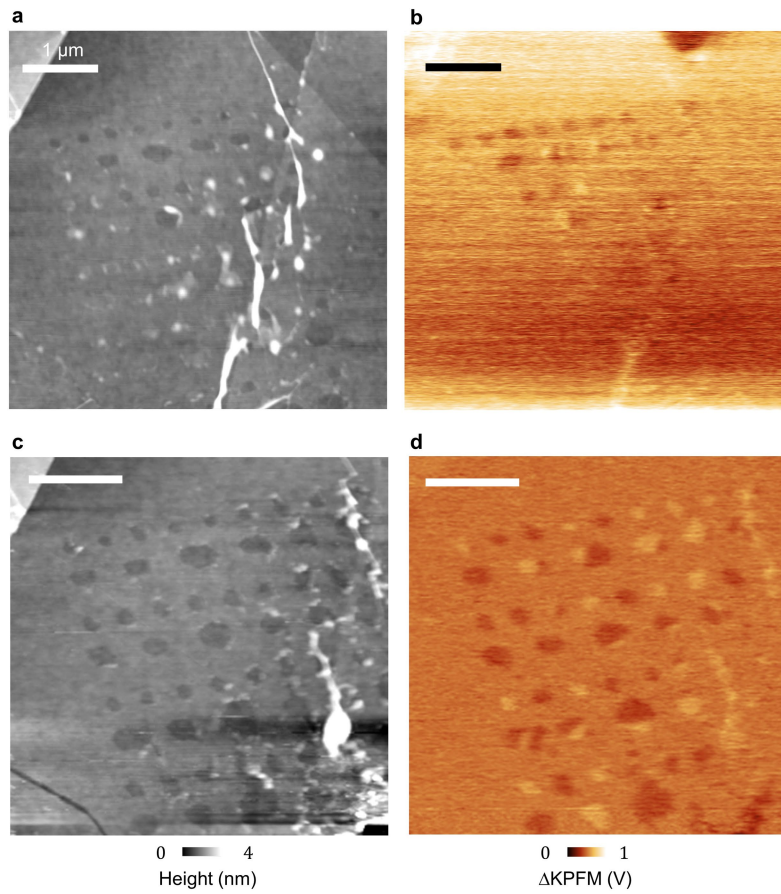


Extended Data Fig. 5 | Triangular intermediate transition states (device 2). **a**, Topographic image of a 250-nm cavity. **b–d**, KPFM image measured before and after applying bias scans as indicated in each map.

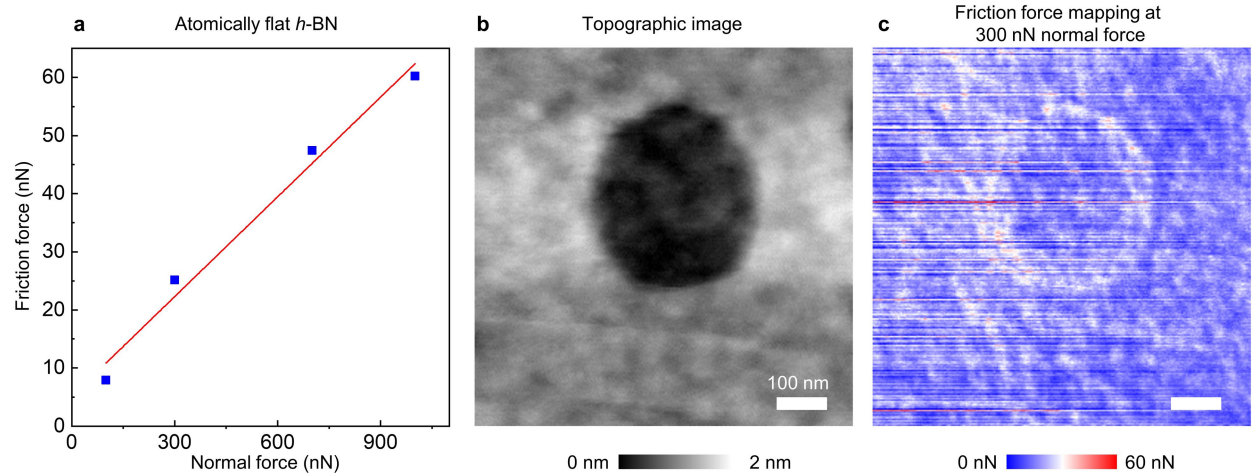


Extended Data Fig. 6 | Determination of threshold pressure for dislocation movement. **a**, Topographic AFM image of the measured array. **b**, KPFM signals before tip pressing. **c**, Successive pressing experiments. Scanning illustration

and applied force indicate the contact-mode scan parameters before the KPFM image. Scale bar indicates $1\mu\text{m}$.



Extended Data Fig. 7 | Imaging sagging of active layers (device 2). **a,b**, Topography and surface potential maps of as-fabricated cavity array. **c,d**, Topographic and KPFM maps after AFM contact-mode scans at a pressure of 300 nN. Scale bars, 1 μm.



Extended Data Fig. 8 | Friction force measurement around the cavity. **a**, Friction force calibration curve measured in atomically flat h-BN. **b**, Topographic image of cavity in device 3 measured at 300-nN loading force. **c**, Corresponding friction force mapping at 300-nN applied normal force.

Article

Extended Data Table 1 | Flakes thickness of the three devices presented in the main text

Device name	h-BN thickness (pick-up, top, bottom)	graphene spacer layers
Device 1: 8.6 nm h-BN	4.3 nm, 2.3 nm, 2.0 nm	Bilayer
Device 2: 4.5 nm h-BN	2.5 nm, 1 nm, 1 nm	Monolayer
Device 3: WSe ₂	4.5 nm, monolayer WSe ₂	Trilayer